Materials Today Advances 29 (2026) 100705

Contents lists available at ScienceDirect

Materials Today Advances

journal homepage: www.journals.elsevier.com/materials-today-advances/

Label-free opto-physicochemical profiling of eosinophils reveals molecular and structural signatures for EGPA diagnosis

Minju Cho [a,1], Joon Seup Hwang [a,1], Ji-Hyang Lee [b], Yu-ra Ha [a], You Sook Cho [c], Chan-Gi Pack [a,d], Jun Ki Kim [a,d,*]

[a] Department of Convergence Medicine, Brain Korea 21 Project, University of Ulsan, College of Medicine, 88, Olympic-ro, 43-gil, Seoul, 05505, Republic of Korea
[b] Department of Allergy and Clinical Immunology, Seoul National University Hospital, Seoul, Republic of Korea
[c] Department of Allergy and Clinical Immunology, Asan Medical Center, University of Ulsan College of Medicine, Seoul, Republic of Korea
[d] Biomedical Engineering Research Center, Asan Medical Center, Seoul, Republic of Korea

ARTICLE INFO

Keywords:
Eosinophilic granulomatosis with polyangiitis
Eosinophil
Optical diffraction tomography
Refractive index
Raman spectroscopy
Machine learning algorithm
Partial least squares discriminant analysis
K-means clustering
Opto-physicochemical

ABSTRACT

Eosinophilic granulomatosis with polyangiitis (EGPA) is a rare disease that requires accurate diagnostic methods to overcome the limitations of current diagnostic criteria relying on clinical observation. Eosinophils from EGPA undergo dynamic changes that reflect its pathological state. Thus, physicochemical analysis of EGPA eosinophils may serve as a key diagnostic approach. In this study, eosinophils from patients with EGPA (n = 8) and healthy control group (n = 7) were analyzed using a multimodal imaging system with aligned optical diffraction tomography (ODT) and Raman spectroscopy. Given that ODT allows for physical analysis and Raman shift indicates chemical components, combining these two different analyses approaches could improve the accuracy of classification. We applied partial least squares discriminant analysis (PLS-DA) on Raman spectrum, specifically focusing on k-means clusters, corresponding to high refractive index (RI) regions identified by ODT. This process aimed to extract variable importance projection (VIP) score, to analyze key feature of Raman spectrum for chemical profiling. Chemical profiling from Raman spectrum complementarily explains the high RI value in granules. These granules enriched areas, derived from ODT physical feature with the validation of Dice-similarity Coefficient, enhanced the accuracy of EGPA prediction up to 96%. This integrated approach demonstrates the potential of multimodal profiling to enhance diagnostic precision for eosinophilic disorders.

1. Introduction

Eosinophilic granulomatosis with polyangiitis (EGPA), known as Churg-Strauss syndrome is a rare disease characterized by small- and medium-vessel vasculitis associated with eosinophil-rich granulomatous inflammation, bronchial asthma, and eosinophilia. EGPA is the rarest form of anti-neutrophil cytoplasm antibody (ANCA)-associated vasculitis (AAV) [1], with an annual incidence of only 0.9–2.4 cases per million individuals [2,3]. EGPA diagnosis typically takes 5–9 years due to the rarity and it is often misdiagnosed as asthma or Nasal allergies, whose symptoms resembles the most prominent symptoms in the early stages of EGPA. Despite its clinical significance, research on EGPA has progressed less extensively compared with other forms of AAV due to its rarity [1]. In 2021, the American College of Rheumatology/Vasculitis Foundation developed guidelines for diagnosing and treating AVV; however, these guidelines are for AVV and not specified for EGPA. Thus, positively scored parameters, such as peripheral blood eosinophil count, obstructive airway disease, asthma, and extravascular eosinophilic inflammation, are used in scoring systems for EGPA diagnosis [4] As EGPA diagnosis relies on the clinical features, a lack of an official diagnostic criterion poses a substantial challenge.

Analyzing the key pathological characteristics of EGPA at the cellular level is essential to overcome the limitations of current diagnostic strategy for EGPA. Eosinophils contain four major granule proteins that are released during degranulation, eliciting immune responses—namely, major basic protein (MBP), eosinophil cationic protein (ECP), eosinophil-derived neurotoxin (EDN), and eosinophil peroxidase (EPO) [5]. Analyzing chemical differences such as changes in protein

* Corresponding author. Department of Convergence Medicine, Brain Korea 21 Project, University of Ulsan, College of Medicine, 88, Olympic-ro, 43-gil, Seoul, 05505, Republic of Korea.
E-mail address: kim@amc.seoul.kr (J.K. Kim).
[1] These authors contributed equally to this work.

https://doi.org/10.1016/j.mtadv.2026.100705
Received 26 August 2025; Received in revised form 4 November 2025; Accepted 30 January 2026

expression or various chemical components can be useful in distinguishing patients with EGPA from controls. On the other hand, analyzing morphological changes in cells can be another clinical approach. A previous study employed parameters such as eosinophil size, granule density, and number of nuclear lobes to evaluate eosinophil activation in patients with allergies [6]. Eosinophils in patients with eosinophilia had a larger diameter than those in healthy controls; however, patients receiving corticosteroid therapy showed a decrease in eosinophil diameter and ECP concentration (μg/L) [6]. These physical differences can serve as an important parameter for diagnosing eosinophilic disorders. Because EGPA shares similar clinical symptoms with other eosinophilic disorders, its diagnosis remains challenging [7]. Thus, both physical and chemical analyses of eosinophils can be performed to enhance the diagnostic accuracy.

Raman spectroscopy is a valuable tool for cell analysis because it allows for the observation of cells and their DNA/RNA contents, as well as the distribution of proteins, and lipid within cells [8]. Additionally, Raman spectroscopy enables molecular evaluation of cells, providing valuable insights into their composition and characteristics without any fluorescence labeling [9]. Raman scattering occurs when matter and light interact, leading to changes in the wavelength of scattered light, depending on the properties of the matter that it interacts with. The frequency of scattered light is directly related to the molecular structure of the matter and the original incident light [10].

Optical diffraction tomography (ODT) belongs to a broader class of quantitative phase imaging(QPI) techniques [11], including phase tomography, tomographic phase microscopy, and quantitative phase tomography, which reconstruct optical path length or phase delay to infer intracellular structure. Among these approaches, ODT is a label-free imaging technique that reconstructs the internal structure of live cells using their refractive index (RI) variations. When light passes through objects such as cells, its polarization and wavelength characteristics change based on the structure of cells and RI. Measuring and interpreting with these altered light properties produce multiple 2D images in z-stack which reconstruct 3D images of cells and RI distribution. ODT is a non-destructive method that allows for an analysis of the internal structure of cells without changing their biological properties [12,13].

Even though ODT enables to perform quantification analysis through RI, density changes, morphological changes, there is limitation to acquire chemical composition such as protein, lipid, DNA or RNA related to the RI. Since eosinophils go through dynamic chemical changes within the granule and cytosols when it is under the pathological condition, chemical composition as well as physical changes should be performed to obtain the characteristics of eosinophils under pathologic condition. Therefore, simultaneous acquisition of identical cells using both ODT and Raman spectroscopy and comparison mutual validation can explain how lipid, protein, RNA, DNA related organic peaks corresponds to the RI changes due to accumulation of EPO, EDN, and MPB in granule [14]. This combined analytical approach enables to correlate the physical and chemical metrics, discovering diagnostic standard and biomarkers that single modality either ODT or Raman spectroscopy cannot reveal.

Recent studies have demonstrated that multimodal imaging has been applied to quantitatively profile cells under various pathological condition such as cancer phenotyping, metastatic potential assessment, drug-response monitoring, and metabolic disease. These studies include the combining structural information from ODT with molecular vibrational spectra from Raman for sensitive discrimination of cellular activation or functional states that are limited to capture with either modality alone. However, most existing work has focused on whole cell level morphological or chemical state differences. To our knowledge, no study has quantitatively resolved pathological activation states of immune cells at the level of intracellular organelles or subcellular granules.

In this study, we focus on EGPA as an immunopathological distinct clinical state and demonstrate that Raman–ODT enables precise discrimination of disease specific activation of eosinophils at the granule-resolved subcellular level. This approach provides insights into the molecular and structural alternation of eosinophils and suggests a potential diagnostic framework for distinguishing pathological eosinophil activation in clinical settings. To achieve this, we aligned Raman spectroscopy and ODT by developing an alignment tool and acquired identical eosinophil images. Eosinophils extracted from healthy donors (control = 7) and patients with EGPA (EGPA = 8) were compared through physical and chemical analyses. For the analysis of identical cells, K-means clustering was used for Raman mapping and the clustered map was compared with RI-rendered images from ODT. K-means clustering partitions Raman shift patterns with similar characteristics into the same cluster, utilizing unsupervised machine learning algorithm [15]. To correlate each K-means cluster of Raman spectrum corresponding to the subcellular compartment derived from RI, we performed binary segmentation which is commonly used in cell imaging contests and biomedical images. This process classifies image pixel as either 0 for background and 1 for the object of interest. Given the predicted mask from each ODT and Raman mapping image, we performed Dis similarity Coefficient (DSC) to quantify the overlaps between images [16,17]. Finally, a diagnostic classification algorithm was developed for EGPA by integrating the Raman shift correlated with physical parameters derived from ODT. To perform this process, we employed Principal Component Analysis (PCA) and partial least squares discriminant analysis (PLS-DA). PCA is non supervised machine learning which is commonly used in complex data set such as Raman spectroscopy to simplify spectrum by data reduction [18]. PLS-DA is supervised learning-based classification extracted latent variables via dimensionality reduction, effectively classifying the groups [19] and explain key peak differences between groups with Variable Importance in Projection (VIP) score. Using this classification application, we separated the data and validate the classification performance using confusion matrix. We demonstrated that the multimodal imaging system enabled the observation of identical eosinophils with two complementary optical modalities, allowing for a more comprehensive physicochemical analysis of eosinophils. We established a machine learning algorithm by integrating the Raman shift and physical parameters from ODT, providing the foundation for a robust diagnostic tool for EGPA as shown in Scheme 1 illustrating overall work flow.

2. Methods

2.1. Ethical considerations

Healthy volunteers and patients with eosinophilic granulomatosis (EGPA), who were recruited through the allergy clinic at Asan Medical Center, following informed consent, donated peripheral blood for human eosinophils. The healthy controls were individuals with no documented history of allergic diseases or other diagnosed eosinophilic disorders, while patients with EGPA were diagnosed EGPA based on clinical observations and eosinophil count. This study was approved by the Institutional Reviewed Board (IRB) of Asan Medical Center (IRB no. 2022-1416).

2.2. Human eosinophil preparation

Healthy volunteers and patients with EGPA donated 10 mL of blood sample, which was collected in Vacutainer tubes with sodium heparin (BD Bioscience, Franklin Lakes, NJ, USA) and centrifuged at 1700 rpm and 25 °C. Red blood cells and granulocytes were separated following treatment with ammonium chloride solution on ice for 10–15 min. To discard erythrocytes, the blood sample was washed with EasySep™ buffer (phosphate-buffered saline containing 2% fetal bovine serum and 1 mM EDTA (Gibco, Carlsbad, CA, USA). Subsequently, eosinophils were treated with the EasySep™ Human Eosinophil Isolation Kit (Stem Cell Technologies, Vancouver, Canada) for immunomagnetic negative selection according to the manufacturer's instruction. Purified eosinophils

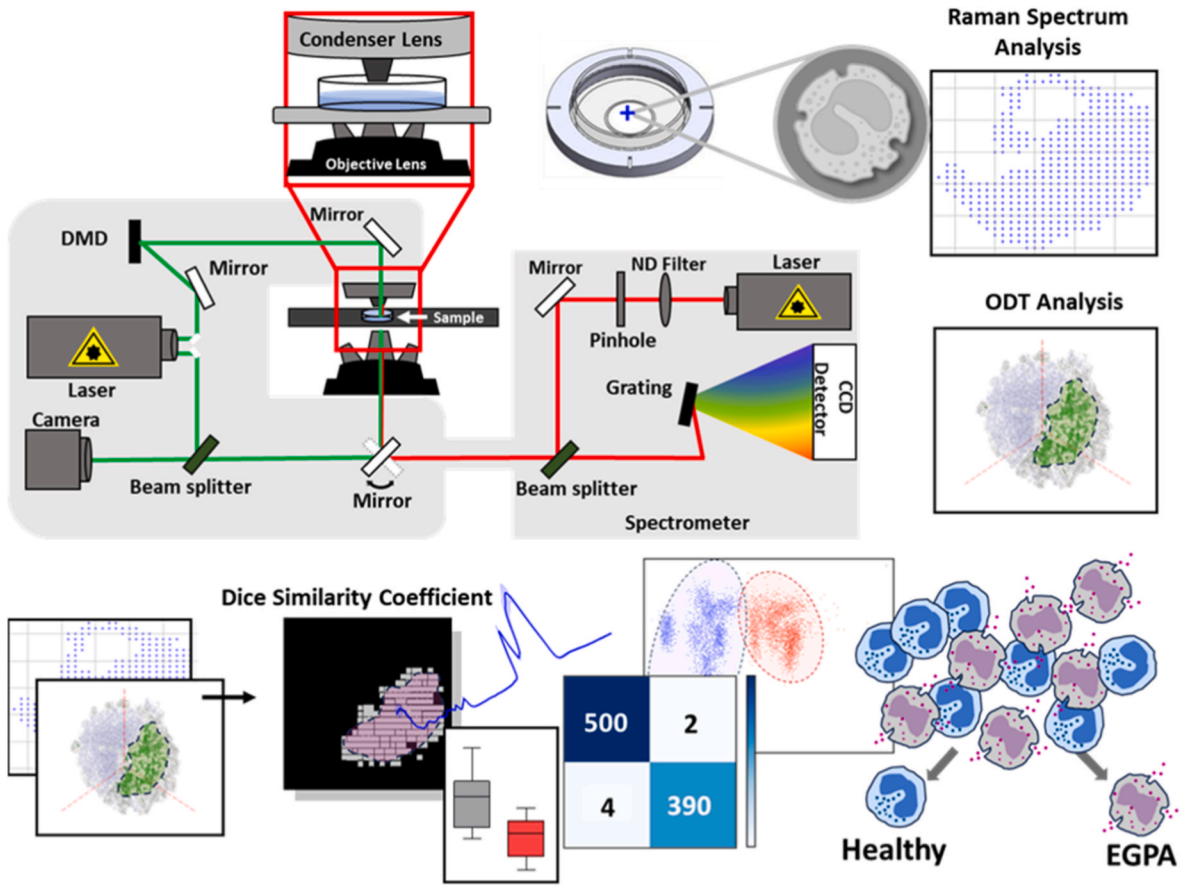

Scheme 1. Over all Schematic image of the optical setup for ODT and Raman Spectroscope with imaging processing for diagnostic approach for EGPA. Using our developed alignment system, identical cells can be observed by both ODT and Raman Spectroscope. After Earning identical cells, each image and data are processed for chemical and physical feature selection before applying opto-physicochemical analysis. physicochemical analysis employment for EGPA diagnosis with the combination of machine learning algorithm. Raman Shifts reveals chemical components while ODT provide physical parameter such as RI or cell volume. Opto-physicochemical analysis on the identical area proved by Dice Similarity Coefficient (DSC) enhances the classification performance and give deeper understanding and high accuracy diagnostic approaches.

were resuspended at a concentration of 4×10^6 cells/mL in RPMI 1640 medium without phenol red, supplemented with 2% fetal bovine serum (Gibco, Carlsbad, CA, USA) [20].

2.3. Alignment of ODT and Raman spectroscopy for the measurement of identical cells

The overall sequential workflow is illustrated in Scheme 1. Our customized-designed three-dimensional (3D) dish holder was fabricated for the sample stage of both the optical diffraction tomography (ODT) and Raman spectroscopy systems. The modular design of the dish holder enables to perform the sequential observation of identical cell by removing outering rings to adjust the specific stage dimensions to each imaging system. A Petri dish fabricated from quartz glass (Ø 12 mm; Fine Plus International, Tokyo, Japan) weas used for a secure mount within the 3D dish holder for all measurements. The scaled quartz Petri dish was used for calibration to ensure precise localization of identical individual cells. The measurement consistency was achieved by computing the spatial offset along the x- and y-axis for the respective coordination of two imaging modalities.

2.4. Label-free ODT imaging process

Three-dimensional imaging of eosinophils was performed using an optical diffraction tomography (ODT) microscope (HT-1H; Tomocube Inc., Daejeon, Korea). The commercial ODT system includes a coherent light source, digital micromirror device, optical field detector, and interferometric module based on Mach-Zehnder configuration. [21]. By interferometrically comparing scattered light with a reference light as light transmits the cellular specimen, the refractive index (RI) distribution of the sample can be reconstructed as 3D hologram images. Eosinophils were immobilized in in quartz glass Petri dishes (Ø 12 mm) under 4% paraformaldehyde fixation prior to imaging. Holographic projections from multiple angles were captured for cellular RI distributions at room temperature of 25 °C [20,22].

2.5. Cell image rendering and quantitative physical analysis

Optical diffraction holographic image and refractive index (RI) rendering of eosinophils were performed using TomoStudio (Tomocube Inc., Daejeon, Korea) for segmenting subcellar structure including the cell membrane, cytosol, nucleus and granules. Based on the RI variation, the software assigns pseudo colors to RI gradients onto virtual palette to facilitate organelle identification and segmentation. [20]. With the physical parameters such as cellular volume, dry mass and intracellular concentration computed from the software, subsequent statistical analysis and data visualizations including box plots was conducted in Python 3.11.22(py11). Using Seaborn and Matplotlib libraries, box plots were generated along with the calculation of student's t-test via SciPy package (SciPy. Stats). Statistical significance was defined as P-values <0.05. P-values are indicated as * if less than 0.05, ** if less than 0.01, and *** if less than 0.001.

2.6. Acquisition of the Raman spectra

Raman microscope with a 100x oil immersion object lens (NA = 0.6, WD = 2.7–4.0 mm; LUCPLFLN40X, Olympus) was used for Raman spectrum acquirement of eosinophils. The excitation source was a 532 nm laser with a 600-groove visual grating. The spectral center was set at 2960 cm^{-1}. The exposure time for each Raman spectrum acquirement was 0.999 s with 100% ND filter application. [23]. All Eosinophils were chemically fixed with 4% paraformaldehyde prior to spectral acquisition on quartz glass Petri dishes (Ø 12 mm) for immobilization of eosinophil and measured at room temperature. Following acquisition, spectral preprocessing was performed to eliminate the background noise. Polynomial baseline correction followed by spectral smoothing for signal enhancement. [24]. This process was achieved using the RAON-Vu (WEVE co. Seongnam, Korea)

2.7. Raman spectral data processing for spectral feature analysis

All Raman spectral processing, visualizing and multivariate analysis were performed with Python 3. 11 (Python Software Foundation, Wilmington, DE, USA) and Visual Studio Code (v1.92, Microsoft, Redmond, WA, USA) using NumPy, Pandas, SciPy, Matplotlib and Scikit-learn libraries. Raw Raman spectrum date were first base line-correction and smoothing process using Savitsky-Golay filter (polynomial order = 3). Each spectrum was then normalized to the intensity of the paraformaldehyde signal at 1040 cm^{-1} [25]. For multivariate classification, Partial Least Squares Discriminant Analysis (PLS-DA) was implemented via scikit-learn PLSRegression (components = 2) for Variable Importance in Projection (VIP) scores.

2.8. Spatial alignment of identical eosinophils using ODT rendering and Raman cluster mapping images

All image processing, segmentation, clustering, and overlap-area calculations were performed in Python (version 3.9) using NumPy, SciPy, scikit-image, CV2 and scikit-learn. First, 2D intensity projection of high RI area of ODT images for binarization via thresholding to generate cell mask. Simultaneously, Raman mapping images were generated by applying K-means clustering (cluster = 8) to produce a pseudo color cluster map and processed binarization of the projected cluster colors correlated with the RI area of ODT. To align the two modalities, we computed a grid translation that maximizes the cross correlation ODT masks and Raman cluster map. Overlapping between two masks was quantified by the Dice Similarity Coefficient (DSC) [16]. This pipeline enabled spatial subcellular chemical cluster with physical morphology at cellular level.

2.9. Machine learning application for EGPA classification

To evaluate the Raman spectrum classification enhancement, we made three classification model for Whole Raman spectrum, Raman spectrum with background removal and Raman spectrum correlated with high RI area in ODT using Principal Component Analysis (PCA) (n = 10) – PLS-DA (n = 2) via PCA from scikit-learn decomposition and PLSRegression from scikit-learn cross decomposition. For each data set were splits into training set (70%) and test set (30%) using scikit-learn model selection. By computing classification accuracy and constructing confusion matrix via scikit metrics. 2D scatter plot of the PC-PLS-DA latent variable were generated Matplotlib.

2.10. Statistical analysis

To compare the physical parameters from ODT and the Raman shift intensity from PLS-DA, we summarized the date into box plot. Each box consists of the interquartile range (IQR) with the middle 50% of the data with the indication of the horizontal median line within the box. The outlier value is shown as individual date points. For the statistical significance between groups, we performed student's t-test using the scipy.stats.ttest in Python. Statistically significance was denoted as * $P < 0.05$, ** $P < 0.01$, and *** $P < 0.001$ indicated above each box plot.

3. Result

3.1. Clinical enrollment and treatment status of study subjects

The patients diagnosed with EGPA and healthy volunteers were enrolled in this study. Healthy volunteers between 18 and 79 years with no history of allergy or any eosinophilic disorders such as asthma, rhinitis or atopy were eligible for enrollment. Individuals who received chronic medical treatment, history of autoimmune disease, or showed eosinophilia (>5%) on blood count are also excluded. Patients with EGPA were diagnosed as those who had the presence of four or more of the following condition such as asthma, peripheral eosinophilia (≥10%), mononeuropathy or polyneuropathy, nonfixed pulmonary infiltrates, paranasal sinus abnormalities, and biopsy evidence of extravascular eosinophilic infiltration according to the 1990 American College of Rheumatology (ACR) classification criteria. Healthy volunteers were 44.7 ± 3.1 years old, with an eosinophil percentage of 2.47 ± 1.42%, an absolute eosinophil count of 185.70 ± 116.50 cells/μL, and a WBC of 7.47 ± 1.23 × 10^3/μL. On the other hand, EGPA patients were 52.7 ± 8.1 years old and exhibited higher eosinophil indices (eosinophil percentage 4.30 ± 3.67%, absolute eosinophil counts 273.50 ± 190.30 cells/μL, and WBC 7.10 ± 1.76 × 10^3/μL) prior to therapy. At the time of sampling, all patients were receiving pharmacologic treatment, and eosinophil measures were reduced (eosinophil percentage 1.20 ± 0.46%, absolute eosinophil count 64.27 ± 31.99 cells/μL, and WBC 5.37 ± 1.29 × 10^3/μL). The pharmacologic treatment that patients were received included inhaled corticosteroids (Fluticasone/Vilanterol, n = 3; Budesonide/Formoterol, n = 3, and biologic therapy (Reslizumab, n = 5). Several patients received combination therapy. Eosinophil samples from EGPA patients were collected during pharmacologic treatment. For medical records, complete blood count (CBC) results from pre-treatment and post-treatment phases of EGPA patients were summarized as well as those of healthy control group in Table S1.

3.2. Acquisition of label-free 3D ODT images for the physical characteristics of eosinophils

Eosinophils were obser**ved using ODT for various physical profiling. In** Fig. 1A and B**, left panel images are raw ODT eosinophil imag**es and the middle panel images are the reconstructed colored images based on the various RI distribution. As the color scale bar is shown and the right side of middle panel images, the highest RI value of control eosinophil is 1.3929 while EGPA eosinophil has the highest RI value of 1.4007 within the granule. To segment eosinophils into subcellular compartment, eosinophils were rendered with pseudo colors overlapping over the area of cytosol, nuclei, and granules based on RI value as shown in the right panel. Comparison of RI values for these subcellular structures between control and EGPA eosinophils revealed that the overall RI value for EGPA eosinophils was higher, as confirmed in the graph depicted in Fig. 1C. However, only the RI value of granules reached statistical significance ($P < 0.001$) while the statistical significance was for cytosol and nucleus were $P = 0.61$ and $P = 0.06$ respectively. Cell volume, surface area, granule volume and dry mass were significantly lower in EGPA eosinophils compared with control eosinophils ($P < 0.01$), from the calculation of 3D hologram images using RI value. However, the cellular component concentration (pg/μm3) of EGPA eosinophils was higher than that of control eosinophils (Fig. S1 A). This suggests that EGPA eosinophils either contained extra internal material or were in a more condensed state. The granule volume was lower in EGPA eosinophils (Fig. S1 B), and the dry mass of granules was also reduced in patients with EGPA (Fig. S1 C).

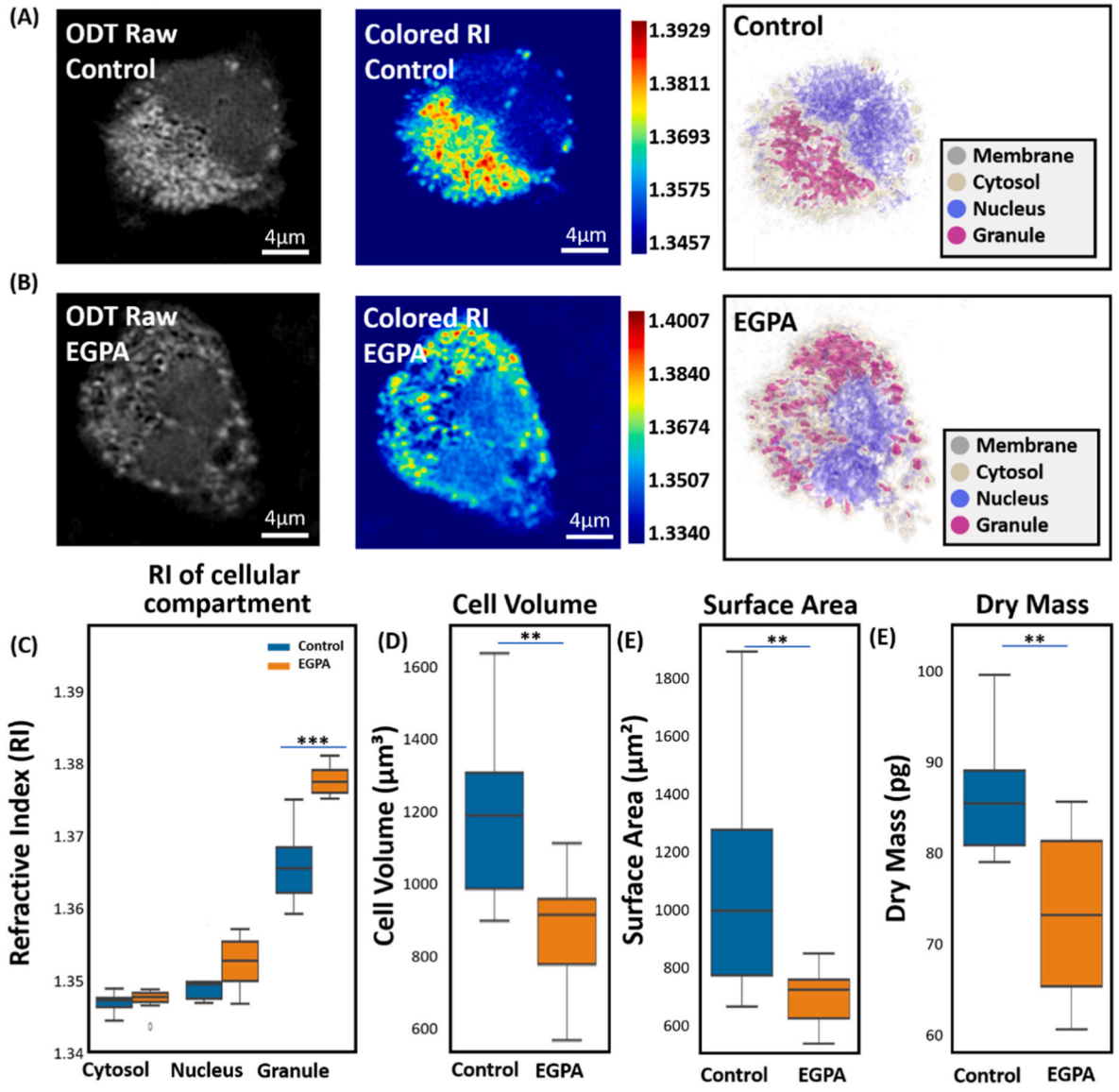

Fig. 1. Physical profiling of individual eosinophils through ODT. (A) Control Eosinophil (B) EGPA Eosinophil represents morphology and RI based rendered images. Left panel shows the raw ODT images. The middle panel shows RI-based rendered images which reconstructed based on different RI values within eosinophil. Red color represents high RI value while blue color represents low RI according to the RI scale bar. Right panel display segmentation images highlighting membrane, cytosol, nucleus, and granules with pseudo colors. (Scale bar = 4 μm) (C) Summarized RI values of cytosol, nucleus, and granules. Cytosol and nucleus RI differences were not statistically significant ($p > 0.05$) while granules showed significant ($p > 0.001$). Summarized box plot of (D) Cell volume (μm^3), (E) Surface Area (μm2) and (F) Dry mass (pg) (n = 7 for control, n = 8 for EGPA eosinophils) (P value: *<0.05, **<0.01, ***<0.001).

However, EGPA eosinophils exhibited a high proportion of granule volume to the cell volume compared to the just granule volume of EGPA as depicted in Fig. S1 D. This observation suggested that granules constituted a larger proportion of the total cell volume in EGPA eosinophils which can be explain for high RI value for granules and higher concentration of the cell. Moreover, granule concentration in Fig. S1 E. also tend to increase which consistent with the elevated granule RI. As shown in Fig. S1 B and C, EGPA eosinophils tended to have smaller value in granule volume and granule dry mass even though there is no statistical significance found. On the other hand, EGPA showed a larger granule volume/cell volume ratio compared with controls. This suggests that EGPA granules occupy proportionally more cell volume despite the small size. Thus, the hallmark characteristics of EGPA eosinophils can be described as granules with higher density relative to their size, and an increased proportion of granules within the total cell volume. Detail quantitative metric values for all parameters are summarized in Table 1.

Table 1
Summary of cellular and granule metrics of control and EGPA eosinophils.

Parameter	Control (Mean ± SD)	EGPA (Mean ± SD)
RI of Cytosol	1.3470 ± 0.0013	1.3474 ± 0.0015
RI of Nucleus	1.3492 ± 0.0021	1.3660 ± 0.0053
RI of Granule	1.3525 ± 0.0034	1.3768 ± 0.0040
Cell Volume (μm^3)	1174.35 ± 263.52	846.26 ± 185.29
Surface Area (μm^2)	1071.09 ± 434.87	673.40 ± 106.57
Dry Mass (pg)	86.40 ± 7.51	73.09 ± 9.66
Cellular Concentration	0.0771 ± 0.0168	0.0925 ± 0.0149
Granule Volume (μm^3)	177.09 ± 77.10	134.50 ± 37.95
Granule Dry mass (pg)	25.44 ± 8.26	21.34 ± 3.31
Granule/Cell Volume ($\mu m^3/\mu m^3$)	0.1493 ± 0.0565	0.1627 ± 0.0410
Granule Concentration	0.1532 ± 0.0286	0.1618 ± 0.0245

3.3. Label-free Raman signal extraction using AI for the diagnostic standard of EGPA

Raman measurements of eosinophils revealed significant differences in Raman shifts between EGPA and control eosinophils. Using whole Raman spectrum, Raman mapping images were produced by normalizing Raman shifts at specific intensity. In Fig. 2A and **B**, bright-field images of eosinophils of control and EGPA are shown on the top panel. Middle panel and bottom panel of Fig. 2A and **B** shows the normalized mapping images at Raman shifts for nucleus (790-810 cm-1) and lipid (2830-2900 cm-1) [26]. All Raman maps were first normalized to the Paraformaldehyde (PFA) peak at 1040 cm^{-1} [25] before generating the intensity mapping. Normalized mapping images based on nucleus signal show no difference between control and EGPA. For Raman mapping image normalized with lipid signal on the other hand, control eosinophil shows concentrated lipid signal within the granule area, producing bright yellow spot against darker background color, while lipid Raman signal is distributed homogenously with broad intensity throughout the granule area. Subsequently, Partial least squares discriminant analysis (PLS-DA) was conducted to extract Variable Importance in Projection (VIP) scores which contribute to the class separation for chemical composition comparison. Using this algorithm, VIP scores with the significance threshold at 1.0 [27] were summarized as Raman shifts graph shown in Fig. 2D and the VIP-selected Raman assignments are summarized in Table 2. The vertical dashed line at 513, 852, 1084, 1707, and 3042 cm^{-} in Fig. 2D represents the significantly exceed the threshold hold of VIP score and these vertical lines are aligned with Raman spectrum as indicated in Fig. 2C. 513 cm^{-} is

Table 2
VIP selected Raman assignment based on PLS-DA.

Raman peak (cm^{-1})	Assignment	Ref.	Raman peak (cm^{-1})	Assignment	Ref.
513	Disulfide bond	[29]	**1438**	Lipid, Fatty Acid	[28]
519	S-S, C-S stretches	[30]	**1539**	Cytochrome C, Heme group	[31]
524	Phosphatidyl serine, s-s disulfide bond	[30, 32]	**1655**	Protein, Amide I	[33]
631	Ring structure, Benzene	[34]	**1707**	Amide I band	[35]
852	Proline, Tyrosine Ring	[35]	**1710**	C=O	[36]
869	Proline	[37]	**2831**	CH symmetric stretching in CH2	[38]
994	Phosphate	[39]	**2836**	C-H	[40]
1084	Phosphodiester bond, DNA	[41]	**2840**	Lipid	[42]
1205	Aromatic amino acid	[43]	**2920**	C-H bond, CH_2 group	[44]
1309	C-C bond	[45]	**3042**	Choline head group	[28]

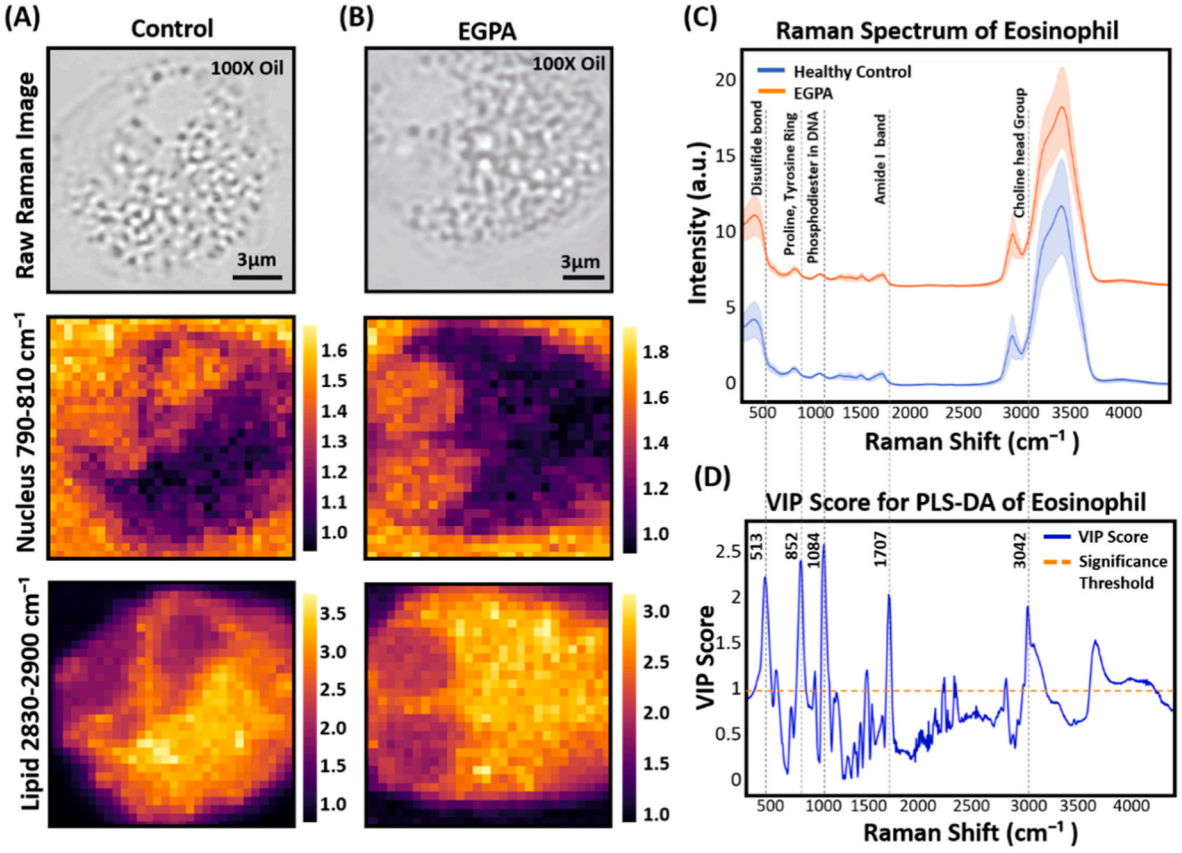

Fig. 2. Raman Spectroscopic characterization of Control and EGPA eosinophils for chemical profiling. (A) control and (B) EGPA each show bright-field images at top panels captured using 100x oil-immersion lens (scale bar = 3 μm) and corresponding Raman mapping images in the middle panels and bottom panels. Middle panel images are Raman mapping images normalized at nucleus Raman signals between 890 and 910 cm^{-1}. Raman mapping Images for bottom panels are normalized at 2830–2990 cm^{-1} for lipid signal. Color scale bar represents normalized intensity (a.u). (C) Raman spectra graph for whole cell including background with Mean ± standard deviation. Mean value is indicated as solid line while standard deviation is shading area. All spectra were normalized to paraformaldehyde peak at 1040 cm^{-1} and (D) Variable Importance in Projection (VIP) score from Partial least squares discriminant analysis (PLS-DA) comparing EGPA to control. The dashed horizontal line marks the VIP threshold of 1.0 for class separation contribution. The dashed vertical lines at VIP score exceeded the significance threshold are aligned on the Raman spectrum with their corresponding chemical assignments.

assigned for S-S bond which can be found in cysteine. 852 cm^{-} is assigned for proline or tyrosine while 1084 cm^{-} is for phosphodiester in DNA. 1707 cm^{-} is Amide I band and 3042 cm^{-} is assigned for choline head group [28] which is abundant in cell membrane. This suggests that control eosinophils and EGPA showed different chemical compositions in DNA, protein and cell membrane within the cell. Although the Raman shifts for lipid signal did not contribute for class separation as listed in the VIP scores, the Raman mapping images clearly showed a distinct distribution of lipid-related Raman signal in EGPA eosinophils compared with control eosinophils.

3.4. Opto-physicochemical characteristics of identical eosinophils

Eosinophils from patients with EGPA showed both physical alterations and Raman shifts changes in chemical composition compared with controls. Identical eosinophils were acquired to integrate

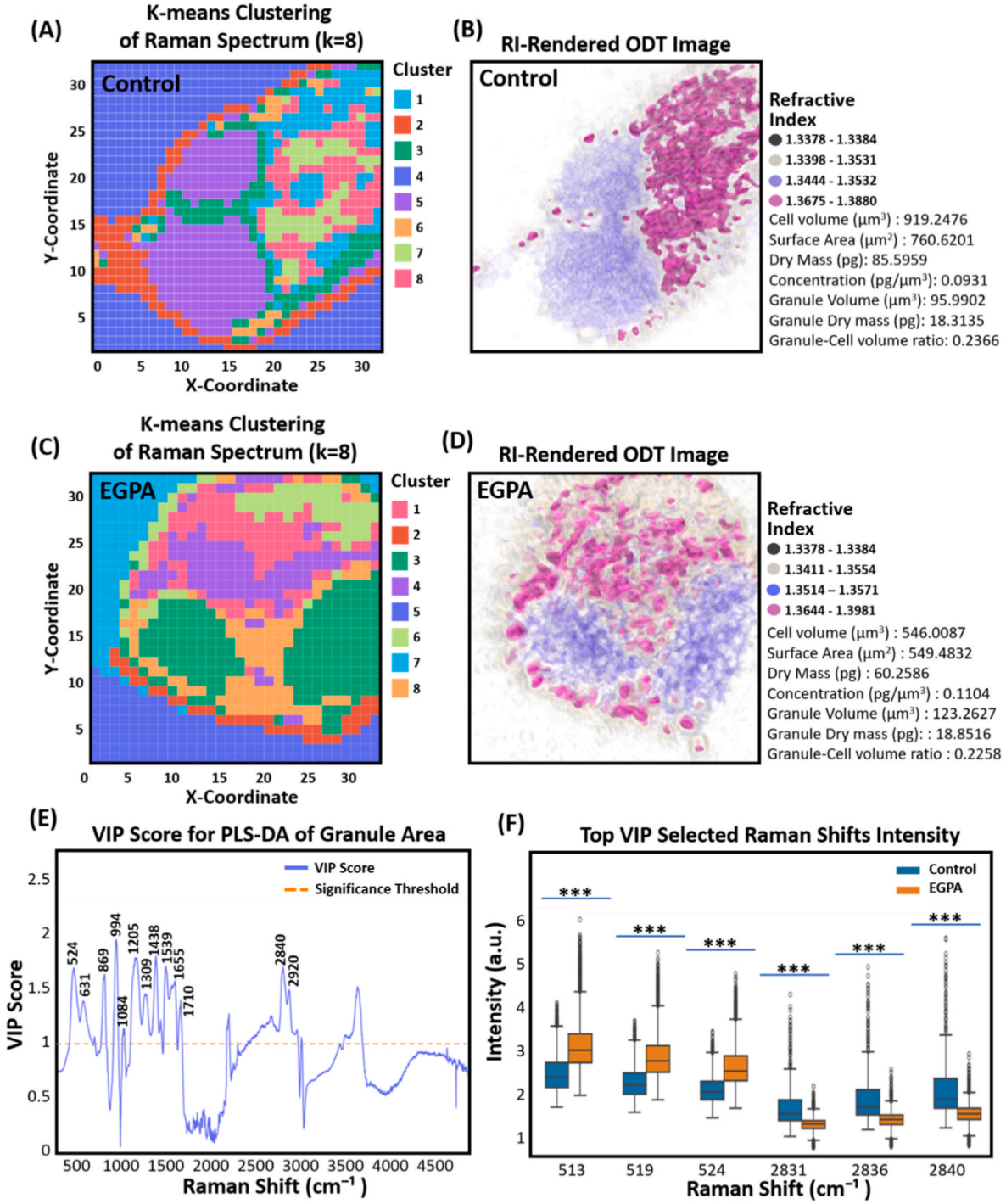

Fig. 3. Multimodal Raman-ODT identical cell profiling for opto-physicochemical evaluation of control and EGPA eosinophils. Raman mapping images through K-means clustering (cluster = 8) are visualized in (A) Control and (C) EGPA. Co-registered Label-free ODT hologram images are shown with RI rendered pseudo color with multiple physical information in (B) Control and (D) EGPA. (E) VIP score is result of PLS-DA for granule area from Raman spectrum corresponding to granule area of ODT images. Horizontal dashed line represents the significance threshold (VIP = 1.0). Raman shifts with the significant VIP score exceeding threshold are indicated. (F) Key biochemical peaks derived from top VIP score were summarized as box plots (***$p > 0.001$).

complementary features for enriched physicochemical analysis at cellular and molecular level. Fig. 3A and **C** show representative K-means clustering Raman mapping images and Fig. 3 B and **D** show ODT rendered images for identical control and EGPA eosinophils, respectively. As the results of physical parameter acquisition through ODT, the RI for all compartment of eosinophil is higher in EGPA compared to control, especially in granule, despite smaller surface area and cell volume. Interestingly, granule concentration in EGPA is higher than control eosinophil, which explain high RI value on granules. Then we performed K-means clustering with k = 8 for segmentation as shown in Fig. 3A and **C**. To quantify spatial coordination between the Raman clusters and RI based compartments from ODT, we first binarized both the granule segmentation from ODT and K-means clusters targeting granule area of eosinophil, since RI of granule was significantly different in control and EGPA. By computing Dice Similarity Coefficient (DSC) for each overlap as graphically described in Fig S2 A, we confirmed that Raman cluster number for 1,7 and 8 for control is complementary to RI value of granule (1.3675–1.3880) by the average of 0.65 DSC. For EGPA, Raman cluster number for 1,4, and 8 is complementary to RI value of granule. (1.3644–1.3981). Dice similarity coefficients were displayed in overlapped images in Fig. S2 B and **C** for control and EGPA respectively.

To define chemical composition of granules exhibiting high RI values, PLS-DA was performed on the Raman clusters overlapped with RI rendered area. Fig. 3E summarizes the results of PLS-DA with VIP scores. The VIP score above the significant threshold is indicated in the graph and the Raman shift assignment is listed in Table 2. Compared with VIP score from the whole Raman spectrum shown in Fig. 3E, granule specific targeted Raman spectrum shows more important Raman peaks, which contribute to the separation data between control and EGPA. Especially lipid related signals 1438, 2840 and 2920 cm^{-1} are shown as VIP score exceeding 1.0. Furthermore, Amide and protein signal such as 869, 1205, and 1655 cm^{-1} were shown to be different between control and EGPA as well as phosphodiester group for 994 and 1084 cm^{-1}. Raman shifts at 1539 cm^{-1} represents for heme group, which represents heme containing enzyme EPO, found in eosinophil granules, is also shown as top VIP score. Then we analyzed which Raman shifts show strong intensity within the top 30 VIP scores. Notably, Raman shifts at 513, 519 and 524 cm^{-1} for disulfide bond showed strong intensity in EGPA while lipid related signal 2831, 2836 and 2840 cm^{-1} showed weaker intensity compared to the control, as summarized in box plot in Fig. 3F.

3.5. *Classification enhancement using dual information from ODT and Raman spectrum*

The following analysis was conducted to classify Raman spectrum of EGPA from control eosinophils, exploring potential possibility of diagnosis based on the found key bio feature. We performed Principal Component Analysis–Partial Least Squares Discriminant Analysis (PC-PLS-DA). We performed 10 principal components in the PCA analysis, and then performed PLS-DA using 2 latent variables on Raman spectrum w/media, Raman spectrum w/o media, and Raman spectrum specifically targeted as highly RI area of ODT for granule area. The data distribution of Raman spectrum is visualized as scatter plot in Fig. 4.

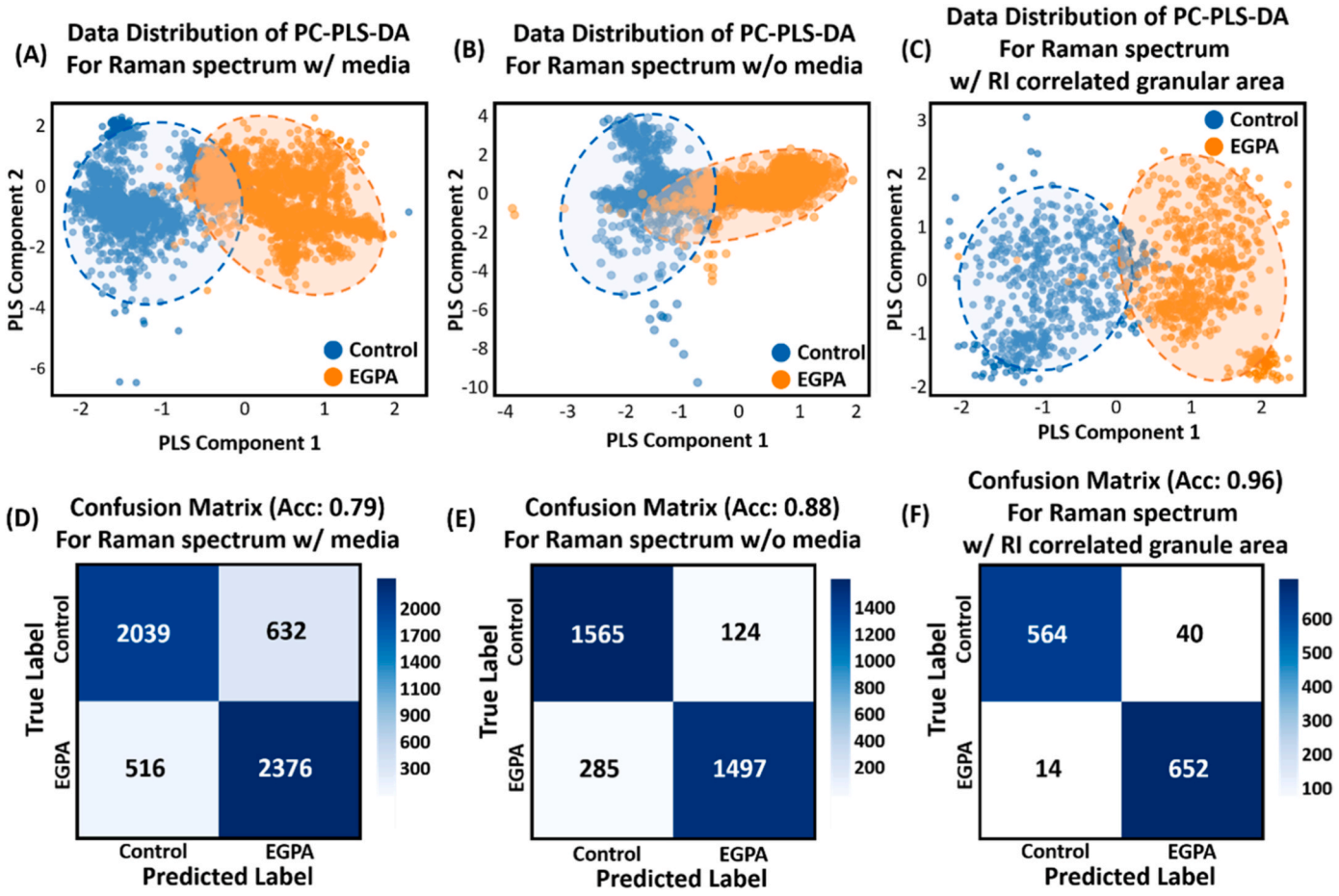

Fig. 4. PCA-PLS-DA classification performance for control and EGPA eosinophils. Data distribution is visualized as scatter plot of (A) Raman spectrum w/media, (B) Raman spectrum w/o media and (C) Raman spectrum w RI correlated granule area for classification enhancement. Dashed-ovals highlight each data point of the control (blue) and EGPA (orange) For (D), (E), and (F) Confusion matrix for classification performance with the ratio of training set 0.7 and test set 0.3 were visualized for Raman spectrum w/media, Raman spectrum w/o media and Raman spectrum with ODT-RI corresponded granule area respectively.

Dashed oval over the scatter points shows a considerable overlap when Raman spectrum data w/media was used for classification in Fig. 4A. However, Raman spectrum w/media contains the background signals which can commonly observed from both control and EGPA. Consider the overlapped scattered as common media signal, we removed Raman signals of media and perform PC-PLS-DA as Raman spectrum w/o media group. As the results, some scatter points are overlapped in Fig. 4B. Finally, we tried PC-PLS-DA on Raman signals with RI correlated granule area. As the results, Raman shifts are were separated between EGPA and control shown in Fig. 4C. Based on this, we tried confusion matrix for classification performance evaluation. The confusion matrix for each classification model is visualized in Fig. 4D, E, and F, and F, and the calculation results for precision, recall, F1-score and accuracy are summarized in Table 3. The accuracy of classification improved markedly from 0.79 to 0.96, through Raman spectrum guided by high area of RI from ODT which are granule area within eosinophils. We also evaluated the consistency of classification performance by performing 5-fold classification validation. As the results, the overall accuracy was 0.97 which consistently showed high classification performance as shown in Fig. S3. The classification report is summarized in Table S2.

4. Discussion

Recent studies have demonstrated that multimodal imaging systems enable the acquisition of a single identical cell for multiple perspective analysis. For instance, SHARE-seq simultaneously profiles both RNA expression and chromatin from the identical cell, whereas Patch-seq integrates cellular imaging, patch-clamp electrophysiology, and transcriptomic profiling of individual neurons, thereby allowing for multimodal analysis of a single cell to reveal correspondences between distinct cell states [46]. A multimodal imaging system combining two-photon microscopy, for obtaining 3D images, and Raman spectroscopy, for monitoring molecular activity to track changes in chemical-associated peak, has also been shown to visualize and quantify cellular metabolic activities [47]. Furthermore, a previous study demonstrated the phenotyping of colon cancer cells according to their state using the combination of phase tomography and Raman spectroscopy [48], implying that the multimodal imaging system integrating physical and chemical analyses can distinguish cellular identities.

Building upon these previous approaches, we performed opto-physicochemical cell profiling using ODT and Raman and gained deep insights into physical and chemical differences, based on the pathological state of EGPA, as compared with control. We focused on how the physicochemical heterogeneity of eosinophils reflects disease specific activation at cellular scaling level for pathological states. To conduct this disease profiling, we demonstrated complementary relationship of information gathered from Raman Spectroscope and ODT, by using the Dice coefficient on cell images to quantify the overlapping regions rather than simply presenting the outputs of each optical modality.

Based on ODT measurement, eosinophils from patients with EGPA have a higher density in the cytoplasm, nuclei, and granules. Notably, the RI of the granules was significantly elevated ($P < 0.05$). Eosinophils from patients with EGPA also exhibited a smaller cell size and lower dry mass than those from healthy controls. Additionally, eosinophils from patients with EGPA showed higher concentration values and reduced surface area, reflecting the increased RI in the cytoplasm, nuclei, and granules and decreased cell size. These results are consistent with the findings of previous studies reporting increased RI values for eosinophil granules in patients with asthma or changes in cell size and nuclear lobe morphology in individuals with allergies [6]. It is important to note that all EGPA samples were obtained from patients having treatment. Therefore, the observed reduction in eosinophil size and dry mass may reflect the effects of corticosteroid or biologic therapy rather than disease-related alterations. Nonetheless, the consistent increase in RI value of granule among patients suggests that structural condensation of eosinophil represents a persistent physicochemical feature associated with disease activity.

Raman spectroscopy reveals the molecular composition difference within eosinophils. For chemical composition analysis, we first generated Raman mapping images by normalizing the whole spectrum to lipid and nucleus signals. Subsequently, we applied PLS-DA to extract VIP scores. With this approach, we found disulfide bonds, phosphatidylcholine signals abundant in the cell membrane, and Amide I and proline bands as well. However, the whole Raman spectrum include background signals. To remove background signals and focus on the meaningful Raman spectrum, we performed K-means clustering to isolate the granule regions corresponding to high RI value in ODT. Given that ODT revealed granule condensation with statistical significance, we hypothesized that those regions show distinct molecular Raman signals in Raman spectra. By performing binary segmentation and dice similarity coefficient calculation, we found the overlapped area of Raman cluster to the high RI in ODT which can complementally explain the output of each modality. The granule targeted analysis produced VIP scores with the wider range of Raman peaks assigned for various molecules such as phosphodiester group, heme group and protein signals. Interestingly, the Raman intensity of disulfide bond peaks at 513, 519, and 524 cm^{-1} is increased in EGPA eosinophils where area lipid-associated peaks at 2831, 2836, and 2840 cm^{-1} were stronger in controls.

Disulfide bond is found in EPO and MBP which are the component of eosinophilic granules within cysteine residues [49,50]. In eosinophils of EGPA patients, inflammation reaction and the accumulation of EOP and MBP within granules increases and as these proteins become highly concentrated in the granules. The cysteine-cysteine disulfide bond signal detected with Raman spectroscope is consistent with the highly condensed RI for granules. This attributed to the relation between the condensed small-volume state of EGPA eosinophils aligns with the disulfide-bond signals in Raman spectrum. In contrast, control eosinophils exhibit a lower overall RI reflecting less condensed state. Since lipid associated Raman peaks showed higher intensity in control while ODT showed the lower RI in granules, the relatively low density of lipid [51] compared with peptide-rich protein explains the correlation of high intensity [52] of lipid in Raman Spectrum and lower RI value on granules.

Then we performed PCA-PLS-DA on the data sets of Raman spectrum w/media, w/o media and the ODT-correlated granule targeted Raman spectrum for classification enhancement evaluation. Among the three classification algorithms models, ODT-correlated-granule-targeted Raman spectrum model is achieved up to 96% accuracy in the confusion matrix with the range of 93–98% for sensitivity, specificity and F1-score. This result confirms that increased RI, morphological changes from ODT, and chemical composition derived from Raman peak intensity are complementary. Their integration can be used to enhance classification performance. This classification model was also evaluated for the robustness of classification performance through 5-fold classification performance which showed the overall accuracy of 0.97. Our work flow sequentially shows combining ODT-Raman multimodal acquisition and overlapping area extraction by Dice based filtering and granule specific VIP analysis. This method offers the foundation of opto-

Table 3
Classification performance of diagnostic model based on confusion metrics.

Model	Class	Precision	Recall	F1-Score
Raman spectrum w/media	Normal	0.80	0.76	0.78
	EGPA	0.79	0.82	0.81
	Accuracy			**0.79**
Raman spectrum w/o media	Normal	0.85	0.93	0.88
	EGPA	0.92	0.84	0.88
	Accuracy			**0.88**
Raman spectrum w/RI correlated granule area	Normal	0.98	0.93	0.95
	EGPA	0.94	0.98	0.96
	Accuracy			**0.96**

physicochemical analysis for various disorders and disease model in different cell types.

While our results indicated highly accurate diagnostic performance of 96% accuracy, this prediction model requires further validation in larger-scale cohort studies. The small sample size (control cell = 7, and EGPA cell = 8) raises potential concerns about overfitting. Although we performed cross-validation and feature selection from PCA followed by PLS-DA, further validation using larger cohort must be performed. Nevertheless, the key point in this study is to emphasize the ability of the multimodal imaging system to provide a comprehensive and multi-date analysis of the individual cell. The accuracy of classification and prediction of disease state can be enhanced through this system, underscoring the potential to distinguish patients with complicated conditions, and monitor responses to drug treatment at the cellular level. Furthermore, although this study primarily focuses on the development of a multimodal Raman–ODT analytical framework, our finding holds meaningful clinical implications. By integrating structural and molecular characterization at the subcellular level, this approach provides a means to link physicochemical imaging with disease phenotyping in a clinically relevant manner. Such granule-resolved physicochemical tracking of eosinophil activation could facilitate the differentiation of diverse eosinophil-associated diseases and enhance the understanding of their underlying immunopathological mechanisms. Because this imaging approach is label-free and non-destructive, it could also be adapted for longitudinal monitoring of disease progression or treatment response. Collectively, these aspects highlight the translational potential of Raman–ODT to bridge single-cell physicochemical analysis with clinical disease profiling.

5. Conclusion

An opto-physicochemical profiling platform was established in this study by integrating ODT and Raman spectroscopy to distinguish eosinophils from EGPA patients and healthy individuals at the cellular level. EGPA eosinophils exhibited higher refractive indices in cytoplasm, nuclei, and granules with smaller volume and dry mass reflecting intracellular condensation. Raman spectrum on the other hand revealed elevated disulfide bond related peak at near 500 cm^{-1} which attributed disulfide bonding occurred granule protein such as EPO and MBP whereas lipid associated peak were prominent in control which reflect the change of molecules between EGPA and healthy eosinophil. This complementary physicochemical analysis included K-means clustering on Raman spectrum to isolate specific clusters corresponding to granule area regions defined by high RI through ODT, validated through Dice coefficient analysis. The RI-correlated granule area of Raman spectrum with the application of PLS-DA model elevated level of 96% classification accuracy from Raman spectrum only with 79 % accuracy, demonstrating the morphological, structural and biochemical information. These finding highlights that the potential of multimodal imaging to improve cellular level analysis for diagnostic approaches in eosinophilic disorders.

CRediT authorship contribution statement

Minju Cho: Writing – original draft, Visualization, Validation, Resources, Methodology, Investigation, Formal analysis, Data curation. **Joon Seup Hwang:** Visualization, Validation, Investigation, Formal analysis, Data curation. **Ji-Hyang Lee:** Writing – original draft, Resources, Investigation. **Yu-ra Ha:** Writing – original draft, Resources, Investigation. **You Sook Cho:** Writing – original draft, Validation, Resources. **Chan-Gi Pack:** Writing – original draft, Validation, Resources. **Jun Ki Kim:** Writing – review & editing, Writing – original draft, Validation, Supervision, Funding acquisition, Conceptualization.

Funding

This research was supported by the National Research Foundation of Korea (NRF) grant funded by the Korea government (MSIT) (RS-2024-00450201, RS-2025-25407039, RS-2025-16071277). This study was also supported by grants (2023IP0071) from the Asan Institute for Life Sciences, Asan Medical Center.

Declaration of competing interest

J.K.K. is a scientific advisor to the startup Apollon Inc. (Korea), which may develop diagnostic devices based on this work. The authors declare no other competing interests.

Acknowledgements

The authors thank the core facility of the Convergence Medicine Research Center for Cellular Imaging, Asan Medical Center, for the use of their shared equipment, services.

Appendix A. Supplementary data

Supplementary data to this article can be found online at https://doi.org/10.1016/j.mtadv.2026.100705.

Data availability

Data will be made available on request.

References

[1] S. Furuta, T. Iwamoto, H. Nakajima, Update on eosinophilic granulomatosis with polyangiitis, Allergol. Int. 68 (4) (2019) 430–436.
[2] S. Fujimoto, et al., Comparison of the epidemiology of anti-neutrophil cytoplasmic antibody-associated vasculitis between Japan and the U.K, Rheumatology 50 (10) (2011) 1916–1920.
[3] M.A. Gonzalez-Gay, et al., The epidemiology of the primary systemic vasculitides in northwest Spain: implications of the chapel hill consensus Conference definitions, Arthritis Rheum. 49 (3) (2003) 388–393.
[4] P.C. Grayson, et al., American college of Rheumatology/European alliance of associations for rheumatology classification criteria for eosinophilic granulomatosis with polyangiitis, Ann. Rheum. Dis. 81 (3) (2022) 309–314, 2022.
[5] R.I. Abu-Ghazaleh, et al., Eosinophil granule proteins in peripheral blood granulocytes, J. Leukoc. Biol. 52 (6) (1992) 611–618.
[6] C.J. Pronk-Admiraal, F.E. van Haaster, P.C. Bartels, Clinical evaluation of changes in the morphology of eosinophils, Clin. Chem. Lab. Med. 40 (1) (2002) 27–31.
[7] G. Emmi, et al., Evidence-based Guideline for the diagnosis and management of eosinophilic granulomatosis with polyangiitis, Nat. Rev. Rheumatol. 19 (6) (2023) 378–393.
[8] N. Uzunbajakava, et al., Nonresonant confocal raman imaging of DNA and protein distribution in apoptotic cells, Biophys. J. 84 (6) (2003) 3968–3981.
[9] A.F. Palonpon, M. Sodeoka, K. Fujita, Molecular imaging of live cells by Raman microscopy, Curr. Opin. Chem. Biol. 17 (4) (2013) 708–715.
[10] D.W. Shipp, F. Sinjab, I. Notingher, Raman spectroscopy: techniques and applications in the life sciences, Adv. Opt Photon 9 (2) (2017) 315–428.
[11] M.H. Jenkins, T.K. Gaylord, Three-dimensional quantitative phase imaging via tomographic deconvolution phase microscopy, Appl. Opt. 54 (31) (2015) 9213–9227.
[12] Y. Park, et al., Measurement of red blood cell mechanics during morphological changes, Proc. Natl. Acad. Sci. U. S. A. 107 (15) (2010) 6731–6736.
[13] J. Lim, et al., High-fidelity optical diffraction tomography of multiple scattering samples, Light Sci. Appl. 8 (2019) 82.
[14] Mussad, S., M. Dourra, and K.C. Thandra, Physiology, major basic protein, in *Statpearls*. 2025, Statpearls Publishing Copyright © 2025, StatPearls Publishing LLC.: Treasure Island (FL).
[15] A. Daniel, et al., Raman mapping of oral tissues for cancer diagnosis, J. Raman Spectrosc. 45 (7) (2014) 541–549.
[16] Y.M. Wong, et al., Machine learning prediction of dice similarity coefficient for validation of deformable image registration, Intelligence-Based Medicine 10 (2024) 100163.
[17] D. Kitaguchi, M. Ito, Correction to dice similarity coefficient formula, Dis. Colon Rectum 67 (5) (2024) e304.
[18] A. Ditta, et al., Principal components analysis of raman spectral data for screening of hepatitis C infection, Spectrochim. Acta Mol. Biomol. Spectrosc. 221 (2019) 117173.
[19] M. Lasalvia, V. Capozzi, G. Perna, A comparison of PCA-LDA and PLS-DA techniques for classification of vibrational spectra, Appl. Sci. 12 (11) (2022) 5345.

[20] S.Y. Kim, et al., Label-free imaging and evaluation of characteristic properties of asthma-derived eosinophils using optical diffraction tomography, Biochem. Biophys. Res. Commun. 587 (2022) 42–48.
[21] D. Kim, et al., Label-free high-resolution 3-D imaging of gold nanoparticles inside live cells using optical diffraction tomography, Methods 136 (2018) 160–167.
[22] M.J. Cho, et al., Influence of chemical and genetic manipulations on cellular organelles quantified by label-free optical diffraction tomography, Anal. Chem. 95 (36) (2023) 13478–13487.
[23] A. Dorosz, et al., Eosinophils and neutrophils-molecular differences revealed by spontaneous raman, CARS and fluorescence microscopy, Cells 9 (9) (2020).
[24] S. Lee, et al., Diagnosis and classification of kidney transplant rejection using machine learning-assisted surface-enhanced Raman spectroscopy using a single drop of serum, Biosens. Bioelectron. 261 (2024) 116523.
[25] S. Mordechai, et al., Possible common biomarkers from FTIR microspectroscopy of cervical cancer and melanoma, J Microsc 215 (Pt 1) (2004) 86–91.
[26] A. Borek-Dorosz, et al., Identification of inflammatory markers in eosinophilic cells of the immune system: fluorescence, Raman and CARS imaging can recognize markers but differently, Cell. Mol. Life Sci. 79 (1) (2021) 52.
[27] J.M. Surmacki, et al., Raman micro-spectroscopy for accurate identification of primary human bronchial epithelial cells, Sci. Rep. 8 (1) (2018) 12604.
[28] C. Lee, C.D. Bain, Raman spectra of planar supported lipid bilayers, Biochim. Biophys. Acta 1711 (1) (2005) 59–71.
[29] S. Mattiello, et al., Physico-chemical characterization of keratin from wool and chicken feathers extracted using refined chemical methods, Polymers 15 (1) (2022).
[30] H.E. Van Wart, et al., Disulfide bond dihedral angles from Raman spectroscopy, Proc. Natl. Acad. Sci. U. S. A. 70 (9) (1973) 2619–2623.
[31] T. Kitagawa, et al., The pH dependence of the resonance raman spectra and structural alterations at heme moieties of various c-type cytochromes, Biochim. Biophys. Acta 494 (1) (1977) 100–114.
[32] S. Wang, et al., Confocal raman microspectral imaging of ex vivo human spinal cord tissue, J. Photochem. Photobiol., B 163 (2016) 177–184.
[33] F. León-Bejarano, et al., Raman spectroscopy study of skin biopsies from patients with Parkinson's disease: trends in alpha-synuclein aggregation from the amide I region, Appl. Spectrosc. 76 (11) (2022) 1317–1328.
[34] P. Wang, et al., Facile detection and quantification of acetamiprid using a portable raman spectrometer combined with self-assembled gold nanoparticle array, Chemosensors 9 (11) (2021) 327.
[35] G. Pezzotti, Raman spectroscopy in cell biology and microbiology, J. Raman Spectrosc. 52 (12) (2021) 2348–2443.
[36] W.M. Scovell, V. Amarnath, A.D. Broom, Raman spectral studies of poly(1-methylinosinic acid), Nucleic Acids Res. 6 (3) (1979) 1049–1061.
[37] N. Stone, et al., Raman spectroscopy for identification of epithelial cancers, Faraday Discuss 126 (2004) 141–157. ; discussion 169–83.
[38] E.J. Jebaseelan Samuel, S. Mohan, FTIR and FT Raman spectra and analysis of poly (4-methyl-1-pentene), Spectrochim. Acta Mol. Biomol. Spectrosc. 60 (1–2) (2004) 19–24.
[39] W.L. Kubasek, B. Hudson, W.L. Peticolas, Ultraviolet resonance Raman excitation profiles of nucleic acid bases with excitation from 200 to 300 nanometers, Proc. Natl. Acad. Sci. U. S. A. 82 (8) (1985) 2369–2373.
[40] B. Tołpa, et al., FT-Raman spectra in combination with machine learning and multivariate analyses as a diagnostic tool in brain tumors, Nanomedicine 57 (2024) 102737.
[41] Y. Chen, et al., Raman spectroscopy analysis of the biochemical characteristics of molecules associated with the malignant transformation of gastric mucosa, PLoS One 9 (4) (2014) e93906.
[42] I.P. Santos, et al., Raman spectroscopic characterization of melanoma and benign melanocytic lesions suspected of melanoma using high-wavenumber raman spectroscopy, Anal. Chem. 88 (15) (2016) 7683–7688.
[43] K.W. Short, et al., Raman spectroscopy detects biochemical changes due to proliferation in mammalian cell cultures, Biophys. J. 88 (6) (2005) 4274–4288.
[44] M. Matthiae, A. Kristensen, Hyperspectral spatially offset Raman spectroscopy in a microfluidic channel, Opt. Express 27 (3) (2019) 3782–3790.
[45] W.T. Cheng, et al., Micro-Raman spectroscopy used to identify and grade human skin pilomatrixoma, Microsc. Res. Tech. 68 (2) (2005) 75–79.
[46] H. Hu, G. Quon, scPair: boosting single cell multimodal analysis by leveraging implicit feature selection and single cell atlases, Nat. Commun. 15 (1) (2024) 9932.
[47] Z. Li, et al., Multimodal imaging unveils the impact of nanotopography on cellular metabolic activities, Chem Biomed Imaging 2 (12) (2024) 825–834.
[48] A. Bresci, et al., Label-free morpho-molecular phenotyping of living cancer cells by combined Raman spectroscopy and phase tomography, Commun. Biol. 7 (1) (2024) 785.
[49] C. Oxvig, G.J. Gleich, L. Sottrup-Jensen, Localization of disulfide bridges and free sulfhydryl groups in human eosinophil granule major basic protein, FEBS Lett. 341 (2–3) (1994) 213–217.
[50] F.F. Dias, et al., Human eosinophil leukocytes express protein disulfide isomerase in secretory granules and vesicles: ultrastructural studies, J. Histochem. Cytochem. 62 (6) (2014) 450–459.
[51] K.R. Feingold, Introduction to lipids and lipoproteins, in: K.R. Feingold, et al. (Eds.), Endotext, South Dartmouth (MA), 2000.
[52] H. Fischer, I. Polikarpov, A.F. Craievich, Average protein density is a molecular-weight-dependent function, Protein Sci. 13 (10) (2004) 2825–2828.